

Tuning of energy gap and photoluminescence behaviour of $\text{Zn}_{0.96}\text{Ni}_{0.04}\text{O}$ nanostructure by Cr substitution

D. Theyvaraju¹ · S. Muthukumar²

Received: 29 June 2016 / Accepted: 14 October 2016 / Published online: 22 October 2016
© Springer Science+Business Media New York 2016

Abstract The Cr-doped $\text{Zn}_{0.96}\text{Ni}_{0.04}\text{O}$ ($\text{Zn}_{0.96-x}\text{Ni}_{0.04}\text{Cr}_x\text{O}$) nanoparticles with different Cr concentrations from 0 to 6 % have been synthesized successfully by sol–gel method. The obtained nanoparticles were systematically characterized by X-ray diffraction, energy dispersive X-ray spectra, scanning electron microscope, Fourier transformation infrared spectroscopy, UV–Vis spectroscopy and photoluminescence spectra. X-ray diffraction patterns revealed that Cr was incorporated into the ZnO crystal lattice without disturbing the original wurtzite crystal structure. The increase of lattice parameters by Cr-doping concluded that both Cr^{3+} and Cr^{2+} ions co-exist, and occupy Zn^{2+} in the ZnO host lattice. The observed higher transmittance, energy gap and emission intensity at Cr = 2 % indicate that this is selected as optimized Cr concentration in the host lattice. The blue shift of energy gap and the variation in intensity and position of emission bands in photoluminescence spectra were discussed based on size and defects density.

1 Introduction

Recently, II–VI semiconductors have been attracted more interest due to their direct wide band gap of 3.37 eV and large exciton binding energy of 60 MeV for various applications such as, spintronics, photonics, optoelectronics, light emitting diodes (LEDs), solar cells, laser diodes, piezoelectric transducers, cosmetics, antibiotic material and gas sensors [1–3]. ZnO is known as direct wide band gap of 3.37 eV at room temperature having great potential in applications in solar cells, gas sensors, photo-catalysis, photo-detectors, photodiodes, optical modulator, chemical and bio-sensors, varistors, transparent thin film transistors, and so forth. In recent times, widespread development on the research of ZnO-based nanomaterials has been encouraged by mutually basic sciences and potential advanced technologies [4, 5].

The presence of transition metal (TM) ions in the host semiconductors guide to an exchange interaction between itinerant s and p electron of host ZnO and d electron of TM ions [6], resulting in versatile magnetic-field-induced functionalities. Of the many magnetic-metals, Ni is an important dopant to achieve Curie temperature (T_C) above room temperature. Among the different TMs, Ni is used as first doping element for ZnO because (i) Ni^{2+} (0.69 Å) and Zn^{2+} (0.74 Å) have the same valence and almost similar radius, (ii) exists with different oxidation states and (iii) have different acceptor properties in a ZnO matrix, thus affecting the electronic surface band structure of ZnO [7, 8]. From UV–Visible spectra, Koseoglu et al. [9] observed that ZnO exhibit an energy gap of 3.13 eV and it is reduced by Ni doping. Al-Harbi et al. [10] reported the blue shift in UV emission in Ni-doped where the Ni dopant generates more electrons that occupy the energy levels located at the bottom of the conduction band. Moreover,

✉ S. Muthukumar
drsmk123@yahoo.co.in

¹ PG and Research Department of Physics, H.H. The Rajah's College (Autonomous), Pudukkottai, Tamil Nadu 622 001, India

² PG and Research Department of Physics, Government Arts and Science College, Melur, Madurai, Tamil Nadu 625106, India

photoluminescence (PL) spectra gave more information regarding the doping elements [11]. In the present studies, Ni doping is limited to 4 % since higher doping of Ni produces the metallic clusters [12] which decrease the charge density of material [13].

The higher doping percentage without metallic cluster is ensured by the doping of two or more favour TM ions [14]. Ionic radius of Cr^{3+} is smaller than Zn^{2+} which create easy to substitute into ZnO crystal structure and induce the ferromagnetism at room temperature and also enhances the green emission [15]. Duan et al. [16] have prepared Cr-doped ZnO nanoparticles through soft chemistry route and studied ferromagnetic properties at room temperature. Trivalent Cr^{3+} ions have $3d^3$ high-spin configurations, which may facilitate to produce a great magnetic moments in the host semiconductors [17] and change microstructure and optical properties of ZnO system.

Among the different preparation techniques, sol–gel is one of the significant techniques because it is a simple and easily reproducible method [18]; provide a control over materials composition at molecular and applicable to large industrial scale fabrication of products at low cost. In the present investigation, the structural and optical properties of Ni-doped ZnO and Ni, Cr co-doped ZnO nanoparticles synthesized by sol–gel method have been examined in details. Moreover, FT-IR and photoluminescence behavior of the synthesized samples have been discussed based the size effect and density of defect states present in the samples.

2 Experimental procedure

2.1 Preparation of $\text{Zn}_{0.96-x}\text{Cr}_x\text{Ni}_{0.04}\text{O}$ ($x = 0, 0.02, 0.04$ and 0.06) nanoparticles

During the preparation of $\text{Zn}_{0.96-x}\text{Cr}_x\text{Ni}_{0.04}\text{O}$ ($x = 0, 0.02, 0.04, 0.06$) nanoparticles, the high purity chemicals (Merc >99 % purity) such as Zinc acetate dihydrate [$\text{Zn}(\text{CH}_3\text{CO}_2)_2 \cdot 2\text{H}_2\text{O}$], Nickel acetate tetrahydrate [$\text{Ni}(\text{CH}_3\text{CO}_2)_2 \cdot 4\text{H}_2\text{O}$], Chromium (II) nitrate hexahydrate [$\text{Cr}(\text{NO}_3)_2 \cdot 6\text{H}_2\text{O}$], N, N dimethyl-formamide (DMF) were used without further purification. The appropriate amount of Zinc acetate and Nickel acetate were dissolved in *N, N* dimethyl-formamide (DMF) one by one under constant stirring for 1 h using magnetic stirrer. Followed by Zinc and Nickel acetates, the appropriate amount of Chromium nitrate was added into the solution under constant stirring for another 1 h.

The prepared homogeneous solution was kept at 60 °C for 1 h under constant stirring to ensure the complete reaction. Then, the resulting sols were evaporated in hot air furnace and dried by micro-oven for 2 h. The dried

precursors were collected and ground in an agate mortar. The same procedure was repeated for other samples preparation. Finally, the collected nanoparticles were annealed at 520 °C under air atmosphere for 2 h followed by furnace cooling. The same procedure is repeated to the remaining samples synthesized with nominal compositions of $\text{Zn}_{0.96-x}\text{Cr}_x\text{Ni}_{0.04}\text{O}$ ($x = 0, 0.02, 0.04$ and 0.06).

2.2 Characterization techniques

The crystal structure of $\text{Zn}_{0.96-x}\text{Cr}_x\text{Ni}_{0.04}\text{O}$ ($x = 0, 0.02, 0.04$ and 0.06) nanoparticles was determined by powder X-ray diffraction technique. XRD patterns were recorded by Rigaku C/max-2500 diffractometer using Cu $K\alpha$ radiation ($\lambda = 1.5406 \text{ \AA}$) at 40 kV and 30 mA from $2\theta = 30^\circ$ to 70° . The topological features and composition of Zn, O, Ni and Cr were determined by energy dispersive X-ray spectrometer on K and L lines. The surface morphology of $\text{Zn}_{0.96-x}\text{Cr}_x\text{Ni}_{0.04}\text{O}$ ($x = 0, 0.02, 0.04$ and 0.06) nanoparticles were studied using a scanning electron microscope (SEM, JEOLJSM 6390).

The UV–Visible optical absorption study was carried out to explore their optical properties. The optical absorption and transmittance were determined using UV–Visible spectrometer (Model: lambda 35, Make: Perkin Elmer) in the wavelength ranging from 300 to 650 nm at room temperature. The chemical bonding existing in $\text{Zn}_{0.96-x}\text{Cr}_x\text{Ni}_{0.04}\text{O}$ ($x = 0, 0.02, 0.04$ and 0.06) nanoparticles was studied by Fourier transform infra red (FTIR) spectrometer (Model: Perkin Elmer, Make: Spectrum RX I) from 400 to 4000 cm^{-1} . The sample used for FTIR studies is in the form of pellets prepared by mixing the nanoparticles with KBr at 1 wt%. The photoluminescence (PL) spectra of $\text{Zn}_{0.96-x}\text{Cr}_x\text{Ni}_{0.04}\text{O}$ ($x = 0, 0.02, 0.04$ and 0.06) nanoparticles have been carried out between the wavelength ranging from 340 to 600 nm under the excitation of Xenon lamp laser with 310 nm line using a fluorescence spectrophotometer (F-2500, Hitachi) at room temperature.

3 Results and discussion

3.1 X-ray diffraction (XRD)—structural studies

Figure 1 illustrates the XRD patterns of $\text{Zn}_{0.96-x}\text{Cr}_x\text{Ni}_{0.04}\text{O}$ ($x = 0, 0.02, 0.04$ and 0.06) nanoparticles synthesized by sol–gel method. All the diffraction peaks could be indexed to hexagonal wurtzite structure of ZnO ($a = 3.2488 \text{ \AA}$, $c = 5.2061 \text{ \AA}$, space group P63mc, 186, JCPDS data card 36-1451) with preferred orientation along (101) plane in all the samples. Diffraction lines of ZnO were broadened, and diffraction broadening was found to be dependent on Miller indices of the corresponding sets of

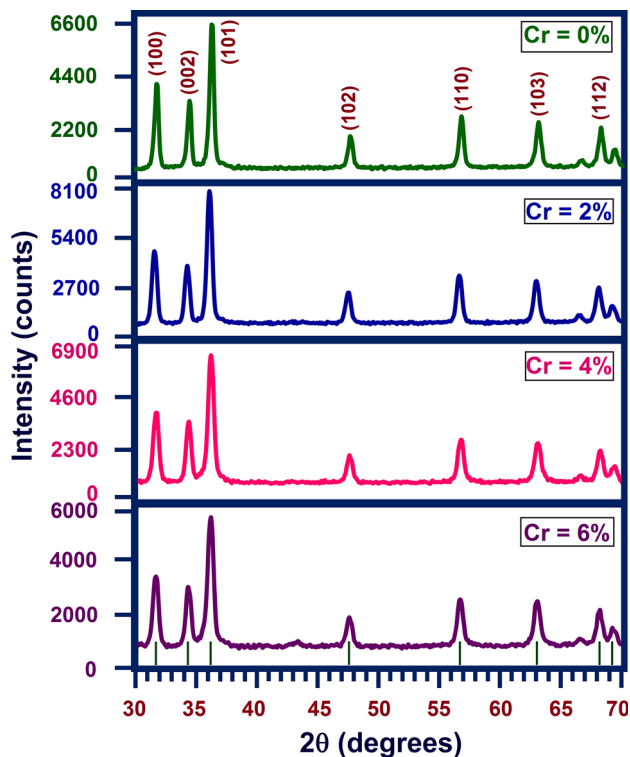


Fig. 1 Room temperature XRD patterns of Cr-doped $\text{Zn}_{0.96}\text{Ni}_{0.04}\text{O}$ nanoparticles with different Cr concentrations from 0 to 6 % between 30° and 70°

crystal plane. It is evident from the XRD spectra that there are no extra peaks corresponding to Ni/Cr, oxides of Ni/Cr or Ni/Cr related secondary and impurity phases which may be attributed to the incorporation of Ni^{2+} and Cr^{3+} instead of Zn^{2+} lattice site. These data indicate that Cr doping does not substantially alter the deposited crystal structure and orientation.

The intensity of (101) plane is magnified in order to analyze the variation of peak intensity. The variation of intensity of $\text{Zn}_{0.96-x}\text{Ni}_{0.04}\text{Cr}_x\text{O}$ nanoparticles from 35.5° to 37° along the (101) plane is shown in Fig. 2a and the variation of peak intensity and crystallite size as a function of Cr concentrations from 0 to 6 % is shown in Fig. 2b. The average crystallite size of the sample is calculated after appropriate background correction from X-ray line broadening of the diffraction peaks of (101) plane using Debye–Scherrer’s formula [19],

$$\text{Average crystallite size (D)} = \frac{0.9\lambda}{\beta \cos \theta} \quad (1)$$

where, λ is the wavelength of X-ray used (1.5406 \AA), β is the angular peak width at half maximum in radian along (101) plane and θ is Bragg’s diffraction angle. The micro-strain (ϵ) can be calculated using the formula [20],

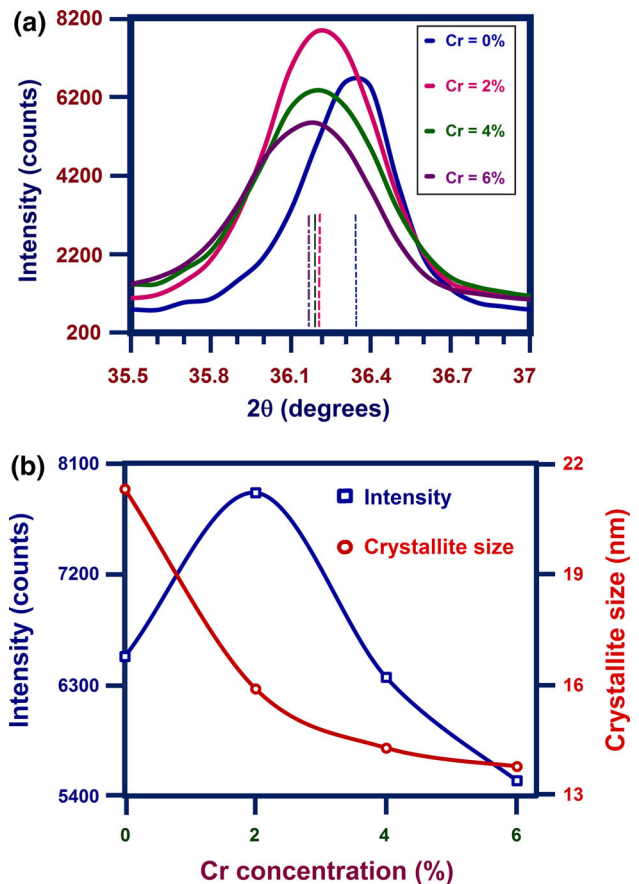


Fig. 2 **a** Variation of XRD intensity along (101) plane between 35.5° and 37° , **b** variation of XRD intensity along (101) plane and crystallite size for different Cr concentration from 0 to 6 %

$$\text{Micro - strain } (\epsilon) = \frac{\beta \cos \theta}{4} \quad (2)$$

With the Cr concentration increasing, the structure of the samples didn’t show any obvious changes, but the diffraction intensity decreased (except Cr = 2 %). The variation in Full width at half maximum (FWHM), peak intensity, average crystallite size (D) and micro-strain (ϵ) along (101) plane of $\text{Zn}_{0.94-x}\text{Ni}_{0.04}\text{Cr}_x\text{O}$ ($0 \leq x \leq 0.06$) nanoparticles are represented in Table 1. The crystallite size calculated from Eq. (1) is decreased from 21.3 nm (Cr = 0 %, without Cr content) to 13.8 nm (Cr = 6 %) by the incorporation of Cr in $\text{Zn}_{0.94}\text{Ni}_{0.04}\text{O}$. The decreasing trend of FWHM and peak intensity by Cr-doping also supports the reduced crystallite size. Moreover, the micro-strain calculated from Eq. (2) is increased from 1.623×10^{-3} (Cr = 0 %) to 2.499×10^{-3} (Cr = 6 %). The noticed higher micro-strain by the incorporation of Cr concentration is due to the decrease of activation energy because electro-negativity of Cr ion is higher than Zn ion [21]. The reduction of activation energy by Cr substitution

Table 1 Full width half maximum (β), peak intensity, average crystallite size (D) and micro-strain (ϵ) along (101) plane of $Zn_{0.94-x}Ni_{0.04}Cr_xO$ ($0 \leq x \leq 0.06$) nanoparticles

Samples	FWHM, β (degrees)	Peak intensity (counts)	Average crystallite size, D (nm)	Micro-strain, ϵ (10^{-3})
$Zn_{0.96}Ni_{0.04}O$	0.391	6532	21.3	1.623
$Zn_{0.94}Ni_{0.04}Cr_{0.02}O$	0.523	7860	15.9	2.171
$Zn_{0.92}Ni_{0.04}Cr_{0.04}O$	0.582	6362	14.3	2.416
$Zn_{0.90}Ni_{0.04}Cr_{0.06}O$	0.602	5524	13.8	2.499

diminishes the crystallite size which results the enhancement in micro-strain [22].

Table 2 represents peak position (2θ), d-value, cell parameters a and c, c/a ratio and volume (V) of $Zn_{0.96-x}Ni_{0.04}Cu_xO$ ($0 \leq x \leq 0.06$) nanoparticles. Generally, the change in lattice parameters depending upon the doping concentration, the defects and stress/strain produced by dopant and the deviation of ionic radii with respect to the substituted matrix ion [23]. The lattice constants a and c are calculated using the following formula used for hexagonal systems [18]:

$$\frac{1}{d^2} = \frac{4}{3} \left(\frac{h^2 + hk + k^2}{a^2} \right) + \frac{l^2}{c^2} \tag{3}$$

where, d is lattice spacing, h, k, l are miller indices. The volume of unit cell of hexagonal system has been calculated from the equation [18],

$$\text{Volume (V)} = 0.866 \times a^2 \times c \tag{4}$$

Yilmaz et al. [24] observed the decrease of lattice parameters upon Cr doping. They demonstrated that the modification in lattice constants may be due to the concentration of foreign atoms and defects, and their difference of ionic radii with respect to the substituted matrix ion ions. Moreover, they concluded that the decrease of lattice parameters is due to the substitution of Cr^{3+} ions (ionic radius $\sim 0.63 \text{ \AA}$) instead of Zn^{2+} ions (ionic radius $\sim 0.74 \text{ \AA}$) in ZnO host lattice. In the present case, the lattice parameters (a and c) of Ni, Cr dual doped ZnO are always greater than Ni-doped ZnO. The increase of lattice

parameters upon Cr-doping suggest that both Cr^{3+} ions with the ionic radius of 0.63 \AA and Cr^{2+} ions with ionic radius of 0.89 \AA co-exist, and occupy Zn^{2+} with ionic radius of 0.74 \AA in the ZnO host lattice [24]. The concentration of Cr^{2+} is considered to be relatively higher which resulting in the larger lattice parameters. The observed constant c/a ratio revealing that there is no change in hexagonal wurtzite structure by Cr value.

3.2 Morphological and compositional studies

Figure 3 shows the SEM images of $Zn_{0.96-x}Cr_xNi_{0.04}O$ nanoparticles with different Cr concentrations from 0 to 6 %. $Zn_{0.96}Ni_{0.04}O$ nanoparticles (Fig. 3a) shows spherical shaped particles with smooth surface morphology where size of the particles ranging from 20 to 30 nm (Table 1). There is no major deviation in shape of the particles upon Cr doping but the size of the nanoparticles is decreased when Cr (2 %, Fig. 3b) is incorporated into host lattice. The observed size deterioration is supported by the results obtained from XRD and the strain analysis (Table 1). Figure 3c and d show a homogenous distribution of the particles with an average particle size of 14 nm.

Chemical compositions of Ni-doped ZnO and Ni, Cr co-doped ZnO were examined by energy dispersive X-ray (EDX) spectroscopy as presented as shown in Fig. 4. The quantitative atomic percentage of the compositional elements such as Zn, O, Ni and Cr in $Zn_{0.96-x}Cr_xNi_{0.04}O$ nanoparticles with different Cr concentrations from 0 to 6 % are presented in Table 3. Table 3 indicates that all the

Table 2 Peak position (2θ), d-value, cell parameters, c/a ratio and volume (V) of $Zn_{0.96-x}Ni_{0.04}Cu_xO$ ($0 \leq x \leq 0.06$) nanoparticles

Samples	Peak position, 2θ ($^\circ$)	d Value (\AA)	Cell parameters (\AA)		c/a Ratio	Volume, V (\AA^3)
			a = b	c		
$Zn_{0.96}Ni_{0.04}O$	36.31	2.4733	3.2473	5.1998	1.6013	47.483
$Zn_{0.94}Ni_{0.04}Cr_{0.02}O$	36.19	2.4802	3.2570	5.2144	1.6009	47.902
$Zn_{0.92}Ni_{0.04}Cr_{0.04}O$	36.17	2.4812	3.2574	5.2162	1.6013	47.931
$Zn_{0.90}Ni_{0.04}Cr_{0.06}O$	36.13	2.4841	3.2622	5.2217	1.6007	48.122

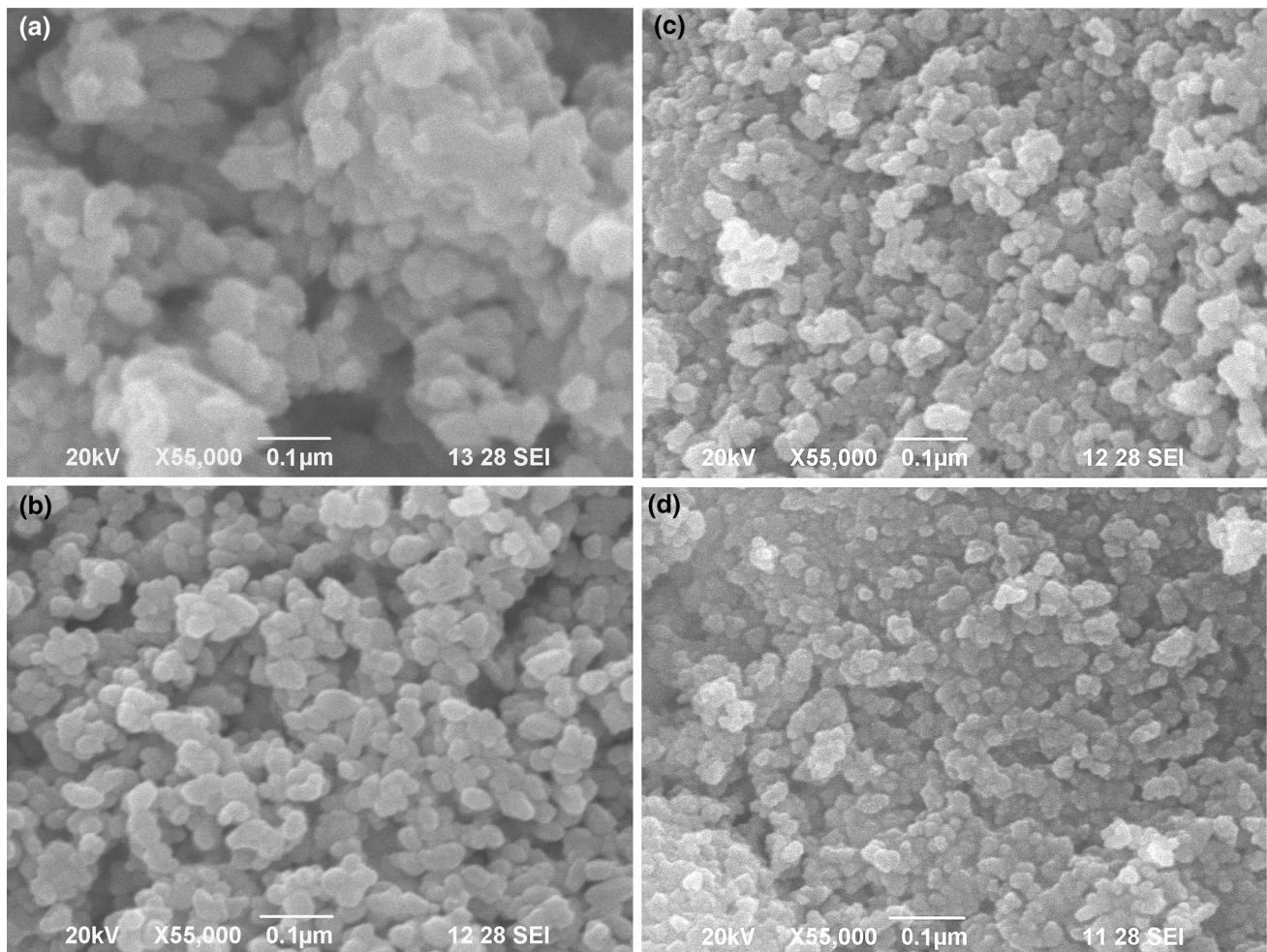


Fig. 3 SEM image of **a** $\text{Zn}_{0.96}\text{Ni}_{0.04}\text{O}$, **b** $\text{Zn}_{0.94}\text{Ni}_{0.04}\text{Cr}_{0.02}\text{O}$, **c** $\text{Zn}_{0.92}\text{Ni}_{0.04}\text{Cr}_{0.04}\text{O}$ and **d** $\text{Zn}_{0.90}\text{Ni}_{0.04}\text{Cr}_{0.06}\text{O}$ nanoparticles

samples are composed of Zn, O, Ni and Cr, demonstrating that the existence of Ni/Cr within the samples as well as the increase in concentration of Cr in the host. It is noticed from Table 3 that actual atomic percentage ratio of Cr is less than the nominal composition in the solution at higher Cr content. The difference between the actual and the nominal Cr concentration is probably due to the dilution of Cr ions in the host matrix. $\text{Ni}/(\text{Zn} + \text{Ni} + \text{Cr})$ ratio is derived to be 4.13, 3.95, 3.96 and 4.02 % respectively, for Cr = 0, 2, 4 and 6 %. Similarly, $\text{Cr}/(\text{Zn} + \text{Ni} + \text{Cr})$ ratio is derived to be 2.19, 3.95 and 5.97 % respectively, for Cr = 0, 2, 4 and 6 %.

3.3 UV–Visible spectra: optical studies

The optical absorption is expected to depend on several factors, such as band gap, oxygen deficiency surface roughness and impurity centers [25]. The optical absorption of $\text{Zn}_{0.96-x}\text{Ni}_{0.04}\text{Cr}_x\text{O}$ nanoparticles with different Cr concentrations from 0 to 6 % was recorded using UV–

Visible spectrometer at room temperature from 300 to 650 nm and shown in Fig. 5.

When Cr is introduced into host the absorption is decreased to its lower value. At Cr = 2 %, the presence of $(\text{OH})^-$ is low which leads the lower stability and causes the reaction to precede much more slowly. Hence, the initial nucleus gets sufficient time to grow. Due to the slowness of the reactions the formation of nucleation centres and hence the absorption is low. At lower Cr concentration (Cr = 2 %), the rapid formation of the ZnO species resulted the faster growth of the ZnO nanostructures. Due to the rapid growth rate, the probability of formation of the defect centres such as Zn interstitials, oxygen vacancy sites decreases which lead the lower absorption.

It is noticed from Fig. 5 that the absorption is increased gradually from Cr = 2 to 4 % and shows maximum value at Cr = 4 %. The increased absorption by Cr doping is due to the created charge carriers. In addition, Cr doping increases the nucleation centres and generates the defect

Fig. 4 Room temperature energy dispersive X-ray (EDX) spectra of **a** $Zn_{0.96}Ni_{0.04}O$, **b** $Zn_{0.94}Ni_{0.04}Cr_{0.02}O$, **c** $Zn_{0.92}Ni_{0.04}Cr_{0.04}O$ and **d** $Zn_{0.90}Ni_{0.04}Cr_{0.06}O$ nanoparticles

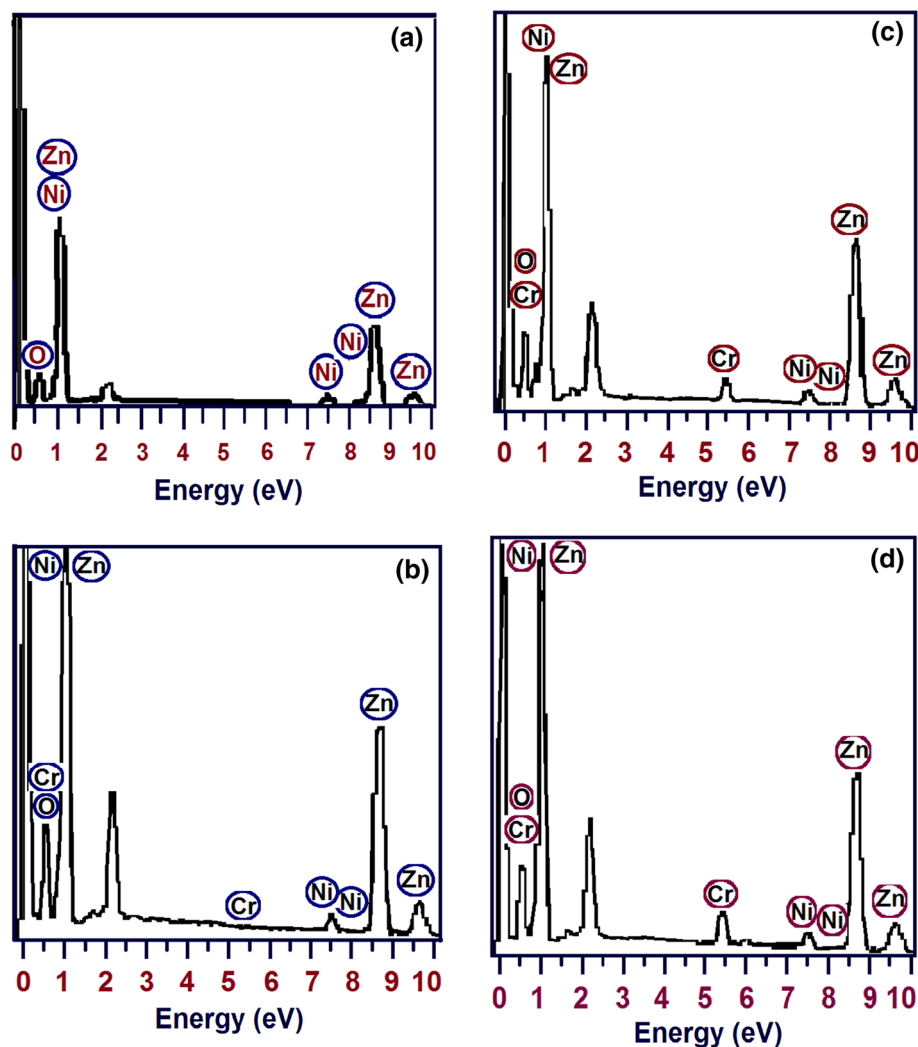


Table 3 The quantitative analyses of atomic percentage of the compositional elements present in $Zn_{0.94-x}Ni_{0.04}Cr_xO$ ($0 \leq x \leq 0.06$) nanoparticles using EDX analysis

Samples	Percentage of the elements (%)					
	Atomic (%)				Ni/(Zn + Ni + Cr) (%)	Cr/(Zn + Ni + Cr) (%)
	Zn	O	Ni	Cr		
$Zn_{0.96}Ni_{0.04}O$	48.08	49.85	2.07	–	4.13	–
$Zn_{0.94}Ni_{0.04}Cr_{0.02}O$	48.27	48.57	2.03	1.13	3.95	2.19
$Zn_{0.92}Ni_{0.04}Cr_{0.04}O$	50.87	44.65	2.19	2.29	3.96	3.95
$Zn_{0.90}Ni_{0.04}Cr_{0.06}O$	50.83	43.53	2.27	3.37	4.02	5.97

states and vacancies which is responsible for the higher absorption. The presence of oxygen deficiencies in $Zn_{0.96-x}Ni_{0.04}Cr_xO$ nanoparticles at higher Cr concentrations are confirmed by EDX spectra. Wang et al. [26] also observed that the doping of Cr ions into ZnO creates more interstitials defects and oxygen vacancies. Increasing Cr concentration from 4 to 6 % increases the nucleation centres and de-generate the defect state and vacancies which is responsible for the decrease of absorption. The observed defects related green band between 482 to 488 nm are due to the oxygen vacancies and intrinsic defects [27].

The room temperature transmittance spectra of $Zn_{0.96-x}Ni_{0.04}Cr_xO$ nanoparticles with different Cr concentrations from 0 to 6 % between 300 to 650 nm are shown in Fig. 6. Cr = 2 % doped sample exhibit higher transmittance and lower absorption. The observed higher transmittance at Cr = 2 % is due to the better optical quality of the crystals. Moreover, the existence of lower defect centres such as Zn interstitials, oxygen vacancy sites, etc. is another possible reason for dominated transmittance. The noticed lower transmittance throughout the region after Cr = 2 % reflected the formation of more

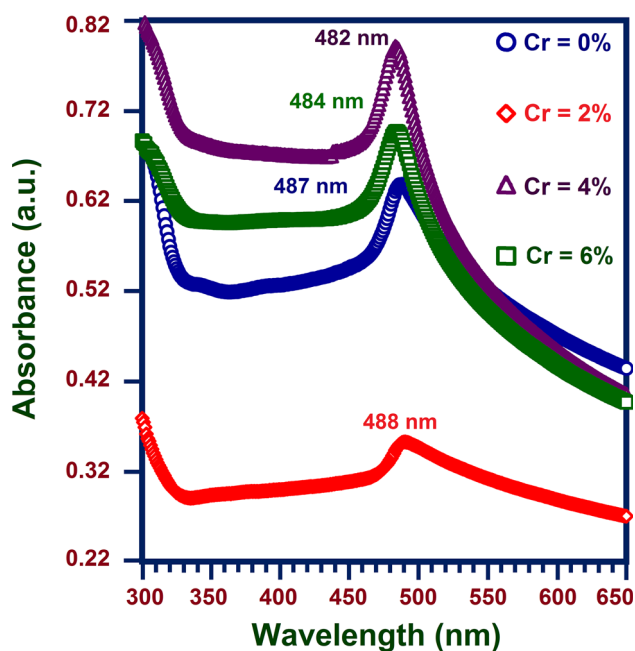


Fig. 5 UV-Visible absorption spectra of Cr-doped $\text{Zn}_{0.96}\text{Ni}_{0.04}\text{O}$ nanoparticles with different Cr concentrations from 0 to 6 % between 300 and 650 nm

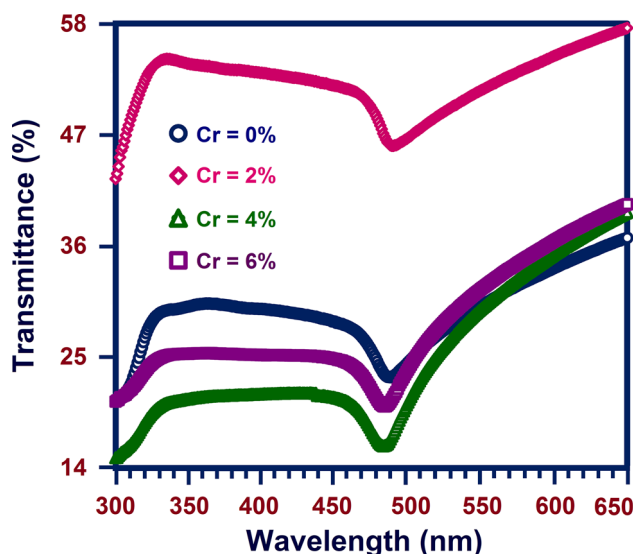


Fig. 6 UV-Visible transmittance spectra of Cr-doped $\text{Zn}_{0.96}\text{Ni}_{0.04}\text{O}$ nanoparticles with different Cr concentrations from 0 to 6 % between 300 and 650 nm

defects such as oxygen vacancies, Zn interstitials and defect related phases.

Tauc's equation is used to find out the optical band gap of $\text{Zn}_{0.94}\text{Cu}_{0.04}\text{Cr}_{0.02}\text{O}$ nanoparticles which demonstrates a relationship between absorption coefficient and the incident photon energy of semiconductors. The optical band gap is evaluated using the Tauc relation [27]:

$$\alpha h\nu = A(h\nu - E_g)^n \quad (5)$$

where, A as a constant, E_g is optical band gap of the material and the exponent n depends upon the type of transition. In the present case, n is taken as 1/2.

The energy band gap of the $\text{Zn}_{0.96-x}\text{Ni}_{0.04}\text{Cr}_x\text{O}$ nanoparticles with different Cr concentrations from 0 to 6 % are calculated with the help of $(\alpha h\nu)^2$ versus $h\nu$ graph as shown in Fig. 7a. The extrapolation of the straight line to the energy ($h\nu$) axis gives the band gap of the material. Figure 7b shows the clear picture of $(\alpha h\nu)^2$ versus $h\nu$ plot for Cr = 2 % samples since it is not clear Fig. 7a. Figure 7c illustrates the variation of energy gap (E_g) as a function of Cr concentrations between 0 and 6 %. The initial substitution of Cr steadily increases the E_g from 3.36 eV (Cr = 0 %) to 3.50 eV (Cr = 2 %, $\Delta E_g = 0.14$ eV). The average crystallite size of $\text{Zn}_{0.96}\text{Ni}_{0.04}\text{O}$ nanoparticles is found to be 21.3 nm which is reduced to 15.9 nm when Cr = 2 % is incorporated into Zn-Ni-O. The above discussion concluded that the degree of crystallinity is the possible reason for the present blue shift of energy gap. The further increase of Cr concentrations decreases the energy gap from Cr = 2 % (3.50 eV) to Cr = 6 % (3.25 eV). Yilmaz et al. [24] observed the analogous energy gap reduction by doping Cr with ZnO. The lattice distortion in ZnO is increased at higher Cr content due to exerting the dopant atoms into wurtzite structure of ZnO [28]. Moreover, the diminution in the energy gap can be ascribed to the transitions between the partially forbidden valance and conduction bands and also due to the exchange interaction between the d electrons of Cr ions [29].

3.4 Fourier transform infrared (FTIR) studies

FTIR is one of the useful techniques to recognize the elemental constituents of a material. Generally, the chemical composition and morphology of the samples are evaluated by peak position and peak intensity [30] of FTIR. Figure 8 illustrates the characteristic peaks exposed by FTIR spectra of $\text{Zn}_{0.96-x}\text{Ni}_{0.04}\text{Cr}_x\text{O}$ nanoparticles with different Cr concentrations from 0 to 6 % between 400 and 4000 cm^{-1} . The IR frequencies along with the vibrational assignments of the above prepared samples assigned at room temperature are presented in Table 4.

The broad band between 3200 and 3600 cm^{-1} represents O-H stretching vibrations of H_2O in Zn-O host lattice [31]. The absorption band around 2819 cm^{-1} is assigned to C-H stretching vibration of residual organic component such as acetate compounds [32]. The Absorption peaks around 2348 cm^{-1} is because of an existence of CO_2 molecule in air [33]. Another sharp peak around 1604 cm^{-1} is attributed to H-O-H bending vibration which is assigned to a small amount of H_2O in the ZnO

Fig. 7 **a** The $(\alpha h\nu)^2$ versus $h\nu$ curves of Cr-doped $Zn_{0.96}Ni_{0.04}O$ nanoparticles with different Cr concentrations from 0 to 6 % for energy gap calculation, **b** the enlarged $(\alpha h\nu)^2$ versus $h\nu$ curves for Cr = 2 % doped sample, **c** variation of energy gap as a function of Cr concentrations from 0 to 6 %

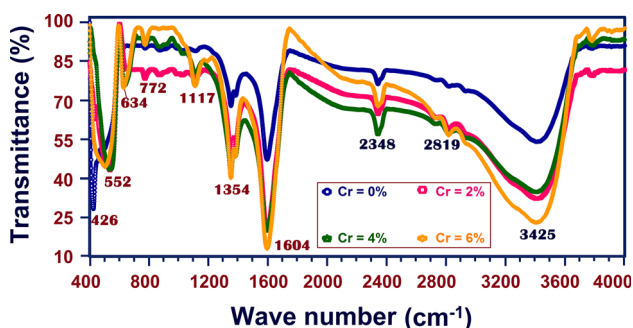
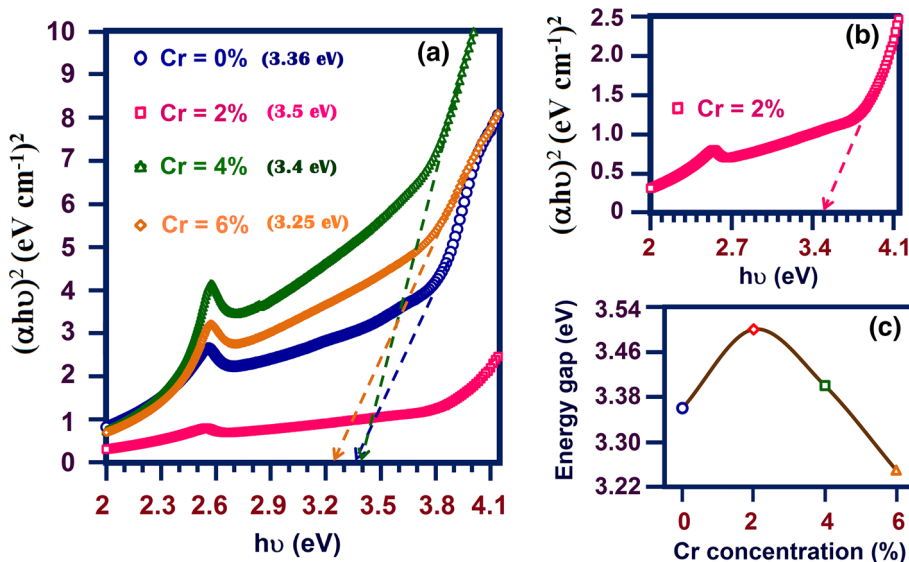


Fig. 8 FTIR spectra of Cr-doped $Zn_{0.96}Ni_{0.04}O$ nanoparticles with different Cr concentrations from 0 to 6 % at room temperature

nanoparticles [34]. The Principal absorption peaks observed 1354 cm^{-1} are corresponding to the symmetric and asymmetric stretching mode of carboxyl group (C=O) [35].

The absorption IR bands between 400 and 1000 cm^{-1} is significant to reveal the presence or absence of Zn–O/Ni–

O/Cr–O/Zn–O–Cr bonds. In order to study the metal-oxide bonds high resolution FTIR spectra from 400 to 1000 cm^{-1} is plotted as shown in Fig. 9. The visible bands below 1000 cm^{-1} represents to metal–oxygen bonds (M–O–M) [36]. The change in intensity and FWHM corresponding to the wave number around 772 cm^{-1} represents the microstructural changes depending on the density of defect states surrounding to Cr/Ni ions in Zn–O lattice. The supplementary feeble absorption peak centered at 634 cm^{-1} representing the metal-oxide phase such as Ni–O/Cr–O found at higher Cr concentration which is not seen in $Zn_{0.96}Ni_{0.04}O$. The stretching of band appearing at 543 cm^{-1} conforms the formation of Zn–O nanoparticles [34]. The shape and size of the ZnO nanoparticles affect the position and intensity of the FTIR peaks [37]. The absorption bands around 426 cm^{-1} (for $Zn_{0.96}Ni_{0.04}O$) and $504\text{--}543 \text{ cm}^{-1}$ (for Cr doped $Zn_{0.96}Ni_{0.04}O$) ascribed to the stretching modes of Zn–O in the octahedral and tetrahedral co-ordination [38], respectively.

Table 4 IR peaks and their assignments of $Zn_{0.94-x}Ni_{0.04}Cr_xO$ ($0 \leq x \leq 0.06$) nanoparticles

Assignments	Wave number (cm^{-1})			
	Cr = 0 %	Cr = 2 %	Cr = 4 %	Cr = 6 %
O–H stretching vibration of H_2O	3425	3429	3426	3425
C–H stretching vibration of residual organic component	2816	2817	2817	2819
Existence of CO_2 molecule in air	2345	2348	2347	2348
H–O–H bending vibration	1602	1600	1604	1602
Symmetric stretching of carboxyl group (C = O)	1353	1350	1352	1354
Micro structural changes	776	772	774	773
Stretching mode of Cu–O	–	648	642	634
Stretching mode of Zn–O	426	542	543	504

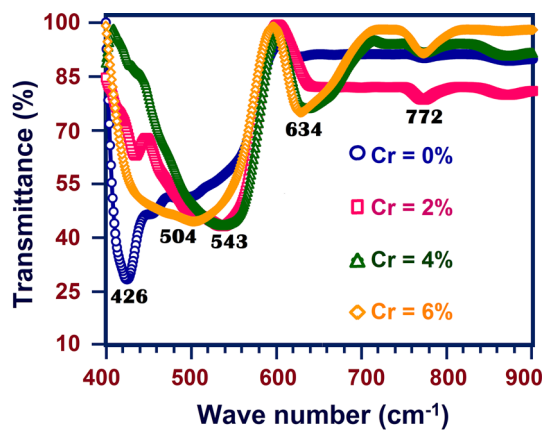


Fig. 9 The enlarged FTIR spectra of Cr-doped $\text{Zn}_{0.96}\text{Ni}_{0.04}\text{O}$ nanoparticles with different Cr concentrations from 0 to 6 % between 400 and 900 cm^{-1}

3.5 Photoluminescence (PL) studies

PL spectra of Ni-doped ZnO ($\text{Zn}_{0.96}\text{Ni}_{0.04}\text{O}$) and Cr, Ni co-doped ZnO ($\text{Zn}_{0.96-x}\text{Ni}_{0.04}\text{Cr}_x\text{O}$) nanoparticles with different Cr concentrations from 0 to 6 % at room temperature are shown in Fig. 10. $\text{Zn}_{0.96}\text{Ni}_{0.04}\text{O}$ nanoparticles exhibit four different emission bands such as 387 nm (UV band), 416 nm (blue band), 479 nm (bluish green band) and 523 nm (green band). When Cr is introduced into $\text{Zn}_{0.96}\text{Ni}_{0.04}\text{O}$ (at lower Cr concentration, 2 %), the intensity of emission bands reached maximum value. Moreover, UV band gets broadened and UV as well as blue bands are merged together. The further increase of Cr concentrations diminishes the emission intensity.

The strong and prominent near band (NB) ultra-violet (UV) emission varies from 357 to 388 nm for different Cr concentrations. The strong UV band is originated from the free excitonic recombination through collision process [39]. It is noticed from Fig. 10 that the peak position of UV emission is shifted towards lower (blue shift) wavelength and also brusquely suppressed at higher Cr concentration. Both blue shift and suppression of UV emission specify that the Cr doping encourage the non-radiative recombination process and also Cr-doping can control the excitonic recombination radiation. The similar results were observed by Liu et al. [40] in Cr-doped ZnO diluted magnetic semiconductor.

No major band shift is noticed for blue band (BB) emission centred at 416 nm but the emission intensity is different for different Cr concentrations. The intrinsic defects and Cr impurity are the source of the blue emission [41]. The blue emission centred at 416 nm corresponds to the relaxation from the excited electrons from the level of interstitial Zn (Zn_i) to extended Zn_i states and transit the valance band with the emission of blue emission. The weak

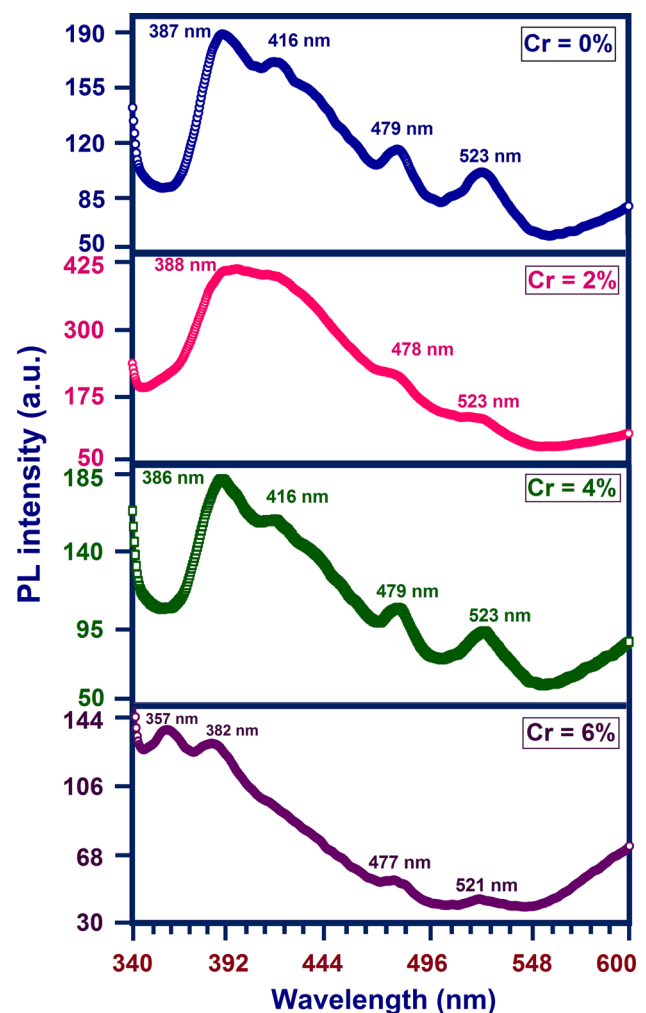


Fig. 10 Room temperature photoluminescence spectra of Cr-doped $\text{Zn}_{0.96}\text{Ni}_{0.04}\text{O}$ nanoparticles with different Cr concentrations from 0 to 6 % between 340 and 600 nm

defect related bluish-green band (BGB) around at 477–479 nm may be accredited to crystalline defects induced during growth and the interaction between oxygen vacancies and interfacial Zn vacancies.

The defect related green band (GB) emission is observed around 521–523 nm whereas intensity is varied depending upon Cr concentrations. The green emission is generally considered to be due to a transition of a photo-generated electron from the conduction band to a variety of deep-level defects [42]. Vanheusden et al. [43] described this green emission by the transition between photo-excited holes and singly ionized oxygen vacancies. It is concluded from this section that the UV emission intensity at room temperature is correlated to a variation of electron concentration [44], whereas the visible emission intensity correlates directly with intrinsic defect densities in the material.

4 Conclusion

Following are the conclusions drawn from the present investigation:

- The Cr-doped $\text{Zn}_{0.96}\text{Ni}_{0.04}\text{O}$ ($\text{Zn}_{0.96-x}\text{Ni}_{0.04}\text{Cr}_x\text{O}$) nanoparticles with different Cr concentrations from 0 to 6 % have been synthesized successfully by the sol-gel method.
- XRD patterns revealed that Cr was incorporated into the ZnO crystal lattice without disturbing the original wurtzite crystal structure.
- The increase of lattice parameters by Cr-doping conclude that both Cr^{3+} and Cr^{2+} ions co-exist, and occupy Zn^{2+} in the ZnO host lattice.
- Chemical composition of the samples was confirmed by energy dispersive X-ray spectra.
- The observed higher transmittance, energy gap and emission intensity at Cr = 2 % indicate that this is selected as optimized Cr concentration in the host lattice.
- The blue shift of E_g and the variation in intensity and position of emission bands in PL spectra were discussed based on size and defects density.

References

- H.K. Yadav, K. Sreenivas, V. Gupta, J.F. Scott, R.S. Katiyar, *Appl. Phys. Lett.* **92**, 122908 (2008)
- C.J. Cong, J.H. Hong, K.L. Zhanga, *Mater. Chem. Phys.* **113**, 435 (2009)
- S. Singh, E.S. Kumar, M.S.R. Rao, *Scr. Mater.* **58**, 866 (2008)
- Z. Zhang, J.B. Yi, J. Ding, L.M. Wong, H.L. Seng, S.J. Wang, J.G. Tao, G.P. Li, G.Z. Xing, T.C. Sum, C.H.A. Huan, T. Wu, *J. Phys. Chem. C* **112**, 9579 (2008)
- Y.Y. Ian Bu, *J. Alloys Compd.* **509**, 2874 (2011)
- Y.S. Wang, P.J. Thomas, P.O. Brien, *J. Phys. Chem. B* **110**, 21412 (2006)
- X. Yan, D. Hu, H. Li, L. Li, X. Chong, Y. Wang, *Phys. B* **406**, 3956 (2011)
- R. Varadhaseshan, S. Meenakshi, Sundar, *Appl. Surf. Sci.* **258**, 7161–7165 (2012)
- Y. Köseoğlu, Y.C. Durmaza, R. Yilginc, *Ceram. Int.* **40**, 10685 (2014)
- T. Al-Harbi, *J. Alloys Compd.* **509**, 387 (2011)
- Y.M. Liu, Q.Q. Fang, M.Z. Wu, Y. Li, Q.R. Lv, J. Zhou, B.M. Wang, *J. Phys. D* **40**, 4592 (2007)
- P.K. Sharma, R.K. Dutta, A.C. Pandey, *J. Magn. Magn. Mater.* **321**, 3457 (2009)
- Y. Wei, D. Hou, S. Qiao, C. Zhen, G. Tang, *Phys. B* **404**, 2486 (2009)
- K.C. Sebastian, M. Chawda, L. Jonny, D. Bodas, *Mater. Lett.* **64**, 2269 (2010)
- L.J. Zhuge, X.M. Wu, Z.F. Wu, X.M. Chen, Y.D. Meng, *Scr. Mater.* **60**, 214 (2009)
- L.B. Duan, X.R. Zhao, J.M. Liu, T. Wang, G.H. Rao, *Appl. Phys. A* **99**, 679 (2010)
- L. Schneider, S.V. Zaitsev, W. Jin, A. Kompch, M. Winterer, M. Acet, G. Bacher, *Nanotechnology* **20**, 135604 (2009)
- D. Theyvaraju, S. Muthukumar, *Phys. E* **74**, 93 (2015)
- M. Ashokkumar, S. Muthukumar, *Powder Tech.* **258**, 157 (2014)
- S. Muthukumar, R. Gopalakrishnan, *Opt. Mater.* **34**, 1946 (2012)
- L.P. Ravaro, D.I. Santos, L.V.A. Scalvi, *J. Phys. Chem. Solids* **70**, 1312 (2009)
- R. Bhargava, P.K. Sharma, S. Kumar, A.C. Pandey, N. Kumar, *J. Solid State Chem.* **183**, 1400 (2010)
- U. Ozgur, Y. Alivov, C. Liu, A. Teke, M.A. Reshchikov, S. Dogan, V.A. Cho, H. Morkoc, *J. Appl. Phys.* **98**, 041301 (2005)
- S. Yilmaz, M. Parlak, Ş. Ozcan, M. Altunbaş, E. McGlynn, E. Bacaksız, *Appl. Sur. Sci.* **257**, 9293 (2011)
- A. Azam, A.S. Ahmed, M.S. Ansari, M. Safeeq, A.H. Naqvi, *J. Alloys Compd.* **506**, 237 (2010)
- B. Wang, J. Iqbal, X. Shan, G. Hung, H. Fu, R. Yu, D. Yu, *Mater. Phys. Chem.* **113**, 103 (2009)
- C. Li, G. Fang, Q. Fu, F. Su, G. Li, X. Wu, X. Zhao, *J. Cryst. Growth* **292**, 19 (2006)
- Y.M. Hu, Y.T. Chen, Z.X. Zhong, C.C. Yu, G.J. Chen, P.Z. Huang, W.Y. Chou, J. Chang, C.R. Wang, *Appl. Surf. Sci.* **254**, 3873 (2008)
- R. Bhargava, P.K. Sharma, A.K. Chawla, S. Kumar, R. Chandra, A.C. Pandey, N. Kumar, *Mater. Chem. Phys.* **125**, 664 (2011)
- Z. Yang, Z. Ye, Z. Xu, B. Zhao, *Phys. E* **42**, 116 (2009)
- K. Nakamoto, *Infrared and Raman Spectra of Inorganic and Coordination Compounds, Parts-A and B* (Wiley, New York, 1997)
- R. Saravanan, K. Santhi, N. Sivakumar, V. Narayanan, A. Stephen, *Mater. Charact.* **67**, 10 (2012)
- M. Arshad, A. Azam, A.S. Ahmea, S. Mollah, A.H. Naqvi, *J. Alloys Compd.* **509**, 8378 (2011)
- A. Jagannatha Reddy, M.K. Kokila, H. Nagabhushana, R.P.S. Chakradhar, C. Sivakumara, J.L. Rao, B.M. Nagabhushana, *J. Alloys Compd.* **509**, 5349 (2011)
- S. Senthilkumar, K. Rajendran, S. Banerjee, T.K. Chini, V. Sengodan, *Mater. Sci. Semicond. Process.* **11**, 6 (2008)
- K. Vivekanandan, S. Selvasekarapandian, P. Kolandaivel, *Mater. Chem. Phys.* **39**, 284 (1995)
- M.A. Verges, A. Mifsud, C.J. Serna, *J. Chem. Soc., Faraday Trans.* **86**, 959 (1990)
- R. Elilarrasi, G. Chandrasekaran, *Mater. Chem. Phys.* **123**, 450 (2010)
- C. Karunakaran, P. Gomathisankar, G. Manikandan, *Mater. Chem. Phys.* **123**, 585 (2010)
- Y. Liu, Y. Yang, J. Yang, Q. Guan, H. Liu, L. Yang, Y. Zhang, Y. Wang, M. Wei, X. Liu, L. Fei, X. Cheng, *J. Solid State Chem.* **184**, 1273 (2011)
- C.H. Zia, C.G. Hu, C.H. Hu, Z. Ping, F. Wang, *Bull. Mater. Sci.* **34**, 1083 (2011)
- L.N. Tong, Y.C. Wang, X.M. He, H.B. Han, A.L. Xia, J.L. Hu, *J. Magn. Magn. Mater.* **324**, 1795 (2012)
- K. Vanheusden, W.L. Warren, C.H. Seagar, D.R. Tallant, J.A. Voigt, B.E. Gnade, *J. Appl. Phys.* **79**, 7983 (1996)
- H.S. Kang, G.H. Kim, S.H. Lim, H.W. Chang, J.H. Kim, S.Y. Lee, *Thin Solid Films* **516**, 3147 (2008)